






Stochastic Electron Acceleration by Temperature Anisotropy Instabilities under Solar Flare Plasma Conditions

Mario Riquelme^{1,5} , Alvaro Osorio¹, Daniel Verscharen^{2,3} , and Lorenzo Sironi⁴ ¹ Departamento de Física, Facultad de Ciencias Físicas y Matemáticas, Universidad de Chile, Chile; marioriquelme@uchile.cl² Mullard Space Science Laboratory, University College London, Dorking, Surrey, UK³ Space Science Center, University of New Hampshire, Durham, NH, USA⁴ Department of Astronomy, Columbia University, New York, NY 10027, USA

Received 2021 March 8; revised 2021 November 16; accepted 2021 November 28; published 2022 January 12

Abstract

Using 2D particle-in-cell plasma simulations, we study electron acceleration by temperature anisotropy instabilities, assuming conditions typical of above-the-loop-top sources in solar flares. We focus on the long-term effect of $T_{e,\perp} > T_{e,\parallel}$ instabilities by driving the anisotropy growth during the entire simulation time through imposing a shearing or a compressing plasma velocity ($T_{e,\perp}$ and $T_{e,\parallel}$ are the temperatures perpendicular and parallel to the magnetic field). This magnetic growth makes $T_{e,\perp}/T_{e,\parallel}$ grow due to electron magnetic moment conservation, and amplifies the ratio ω_{ce}/ω_{pe} from ~ 0.53 to ~ 2 (ω_{ce} and ω_{pe} are the electron cyclotron and plasma frequencies, respectively). In the regime $\omega_{ce}/\omega_{pe} \lesssim 1.2$ – 1.7 , the instability is dominated by oblique, quasi-electrostatic modes, and the acceleration is inefficient. When ω_{ce}/ω_{pe} has grown to $\omega_{ce}/\omega_{pe} \gtrsim 1.2$ – 1.7 , electrons are efficiently accelerated by the inelastic scattering provided by unstable parallel, electromagnetic z modes. After ω_{ce}/ω_{pe} reaches ~ 2 , the electron energy spectra show nonthermal tails that differ between the shearing and compressing cases. In the shearing case, the tail resembles a power law of index $\alpha_s \sim 2.9$ plus a high-energy bump reaching ~ 300 keV. In the compressing runs, $\alpha_s \sim 3.7$ with a spectral break above ~ 500 keV. This difference can be explained by the different temperature evolutions in these two types of simulations, suggesting that a critical role is played by the type of anisotropy driving, ω_{ce}/ω_{pe} , and the electron temperature in the efficiency of the acceleration.

Unified Astronomy Thesaurus concepts: [Solar flares \(1496\)](#); [Space plasmas \(1544\)](#)

1. Introduction

The mechanism responsible for electron acceleration in solar flares is a longstanding open problem in solar physics (see Miller et al. 1997; Benz & Gudel 2010; Fletcher et al. 2011; Benz 2017; Oka et al. 2018; Dahlin 2020; Li et al. 2021 for reviews). Magnetic reconnection within prominent magnetic loops in the solar corona is thought to be the primary process for converting magnetic energy into kinetic plasma energy (Forbes 2013; Miller 2013; Su et al. 2013; Zhu et al. 2016; Gou et al. 2017; Li et al. 2017; Wang et al. 2017; Cairns et al. 2018). However, the dominant mechanism by which electrons are accelerated and the conditions under which it operates remain to be fully understood.

The leading candidate for the location of the acceleration is the reconnection current sheets (CS), where multiple processes are expected to be relevant, including convective and magnetic-field-aligned electric fields (Kliem 1994; Drake et al. 2005; Egedal et al. 2012; Wang et al. 2016) and Fermi-type reflections in coalescing and contracting plasmoids formed by the tearing-mode instability of the CS (Drake et al. 2006, 2013; Le Roux et al. 2015; Du et al. 2018). Recent kinetic simulations are showing that electron spectra with nonthermal power-law tails consistent with observations can be produced within the reconnecting CS (Li et al. 2019; Che & Zank 2020; Che et al. 2021; Arnold et al. 2021; Zhang et al. 2021), and the role played

by plasma conditions in this acceleration (e.g., plasma β and guide field strength) is currently under investigation (see Li et al. 2021 and Dahlin 2020 for recent discussions of the open questions).

Additionally, there is observational evidence suggesting that part of the electron acceleration can also occur outside the CS, in a so-called above-the-loop-top (ALT) region, located between the bottom of the CS and the top of the magnetic loops (e.g., Liu et al. 2008; Chen et al. 2020, 2021). This region constitutes a highly dynamic environment where a significant fraction of the energy carried by the reconnection outflow is dissipated, opening the possibility for several electron acceleration processes to occur. For instance, as the reconnection outflows impinge upon the top of the flare loops, a termination shock (TS) can form (Chen et al. 2019; Luo et al. 2021), potentially giving rise to efficient diffusive shock acceleration (Chen et al. 2015). Also, magnetohydrodynamic (MHD) simulations show that the plasmoids formed in the reconnection CS can generate a highly turbulent TS downstream medium (Takasao et al. 2015; Shen et al. 2018; Cai et al. 2019; Kong et al. 2020). This turbulent environment has been considered as a possible site for efficient stochastic electron acceleration driven by various plasma waves, including fast magnetosonic waves (Miller et al. 1996; Miller 1997; Pongkitivanichakul & Chandran 2014) and whistler waves (Hamilton & Petrosian 1992; Petrosian & Liu 2004). In these models, the waves are generated by MHD turbulence cascade, and their acceleration efficiencies rely on various assumptions, such as the amplitude and spectral energy distribution of the relevant modes (Petrosian 2012; Klein & Dalla 2017).

In addition to being driven by the turbulent cascade, it has been proposed that stochastic acceleration may also be due to

⁵ Corresponding author.

waves excited by electron temperature anisotropy instabilities (Melrose 1974). In this scenario, the temperature anisotropy may be caused by local variations of the turbulence magnetic field, which can make the electron distribution anisotropic due to the adiabatic invariance of the electron magnetic moment μ_e ($\propto v_{e,\perp}^2/B$, where $v_{e,\perp}$ is the electron velocity perpendicular to the magnetic field \mathbf{B} and $B = |\vec{B}|$).

In this work, we build upon this idea and use 2D particle-in-cell (PIC) simulations to study the possible role of electron anisotropy instabilities in stochastically accelerating electrons in ALT regions. We consider the case where the temperature perpendicular to the magnetic field \mathbf{B} ($T_{e,\perp}$) is higher than the parallel temperature ($T_{e,\parallel}$). In addition to the possibility that this anisotropy is produced by local magnetic field growth due to turbulence, $T_{e,\perp} > T_{e,\parallel}$ can also be due to the fact that ALT regions can act as magnetic traps. Indeed, the increase of the magnetic field of the loops toward the solar surface should produce a magnetic mirror that traps large pitch-angle electrons, probably forming an anisotropic “loss-cone” electron velocity distribution with $T_{e,\perp} > T_{e,\parallel}$ (e.g., Fleishman & Melnikov 1998). In addition, these traps are expected to behave as “collapsing traps” as newly reconnected magnetic field lines tend to pile up on the top of the magnetic loops, producing an overall growth of the magnetic field within them. This magnetic growth may also contribute to the increase of the $T_{e,\perp} > T_{e,\parallel}$ anisotropy, as has been shown by previous test particle studies of electron evolution in collapsing traps (Karlicky & Kosugi 2004; Minoshima et al. 2010; Xia et al. 2020). Despite these considerations, there is no direct observational evidence of a $T_{e,\perp} > T_{e,\parallel}$ temperature anisotropy in ALT regions to date, and, therefore, the generation of this anisotropy is an assumption in our work.

Our study is in part motivated by previous PIC simulation studies of temperature anisotropy instabilities in regimes similar to solar flares, where nonthermal electron acceleration has been found (Gary et al. 2011; Chang et al. 2013; Tao & Lu 2014; An et al. 2017; Lee et al. 2018; Abdul et al. 2021). In these studies, arbitrary values for the initial $\Delta T_e/T_{e,\parallel}$ ($\equiv (T_{e,\perp} - T_{e,\parallel})/T_{e,\parallel}$) are imposed in the simulations, with the chosen value of the anisotropy playing a critical role in determining the efficiency of the acceleration (see, e.g., Tao & Lu 2014 where the generation of kappa distributions is found, with the κ -parameter depending on $\Delta T_e/T_{e,\parallel}$). In our simulations, we adopt a different approach by driving the anisotropy through an (externally imposed) magnetic field growth. Including this driving is important because it allows $\Delta T_e/T_{e,\parallel}$ to be limited by the anisotropy threshold for the growth of the unstable modes, which is an important aspect in the evolution of $\Delta T_e/T_{e,\parallel}$ in real systems. Indeed, the existence of these thresholds has been predicted by plasma kinetic theory (e.g., Gary & Cairns 1999) and it has been verified by previous PIC simulations (e.g., Riquelme et al. 2015, 2016, 2017, 2018; Sironi 2015; Sironi & Narayan 2015), and by in situ measurements in the solar wind (e.g., Stverak et al. 2008). In addition, including the anisotropy driving allows the simulations to capture in a self-consistent way the long-term effects of the unstable modes on the nonthermal component of the electron velocity distribution and vice versa, as has been shown by previous PIC studies regarding semirelativistic plasmas relevant for hot accretion flows around black holes (Riquelme et al. 2017; Ley et al. 2019).

Our approach thus is to drive the growth of a $T_{e,\perp} > T_{e,\parallel}$ anisotropy by externally imposing a macroscopic plasma motion that continuously amplifies the local magnetic field due to magnetic flux freezing. After the anisotropy reaches the threshold for the growth of the unstable modes, these modes pitch-angle scatter the particles, maintaining the anisotropy at a self-regulated level and modifying the electron velocity distribution. One of our goals is to understand the sensitivity of the electron acceleration to the type of anisotropy driving. In our runs, we therefore force the growth of the field by imposing either a shearing or a compressing plasma motion (hereafter, shearing and compressing simulations, respectively). We show below that the acceleration efficiencies obtained from these two driving strategies are significantly different.

Some relevant considerations regarding our simulation strategy are described here. (i) Although our simulations include slow (MHD-like) bulk plasma velocities, the simulation domains are much smaller than typical MHD length scales. In this way, our runs focus on the microphysics of the interaction between electrons and the unstable plasma modes by zooming in on the kinetic length scales of the modes (typically close to the electron Larmor radius R_{Le}), and taking the MHD evolution as an external driver. (ii) Our simulations use homogeneous domains with periodic boundary conditions. This means that we do not account for the loss of small pitch-angle electrons, as expected from magnetic trap configurations, and we therefore ignore the possible formation of a loss-cone velocity distribution. (iii) In order to optimize our computational resources, we assume infinitely massive ions. In this way, only the electron-scale dynamics is captured, with the immobile ions only providing a neutralizing charge density to the plasma.⁶

This manuscript is organized as follows. In Section 2 we describe our simulations setup. In Section 3 we use shearing simulations to show how the instabilities regulate the electron temperature anisotropy. In Section 4 we use shearing simulations to show the way in which the instabilities produce nonthermal electron acceleration. In Section 5 we show the compressing case, emphasizing the differences and similarities with the shearing runs. In Section 6 we briefly discuss the possible role of Coulomb collisions. Finally, in Section 7 we present our conclusions.

2. Simulation Setup

We use the PIC code TRISTAN-MP (Buneman 1993; Spitkovsky 2005). Our 2D simulation boxes consist of an initially square domain in the x - y plane, which initially contains a homogeneous plasma with an isotropic Maxwell-Boltzmann velocity distribution in presence of an initial magnetic field $\mathbf{B}_0 = B_0 \hat{x}$. The magnetic field is then amplified by imposing either a shearing or a compressing bulk motion on the particles, which drives the electron temperature anisotropic with $T_{\perp,e} > T_{\parallel,e}$ due to μ_e conservation. In the shearing case, the plasma velocity is given by $\mathbf{v} = -sxy\hat{y}$, where x is the distance along \hat{x} and s is the constant shear rate (this setup is shown in Figure 1 of Ley et al. 2019).⁷ From flux conservation, the

⁶ As was done in a previous study of electron acceleration by temperature-anisotropy-driven instabilities in the context of semirelativistic plasmas, relevant for accretion flows around black holes (Riquelme et al. 2017).

⁷ The shear simulations are performed in the “shearing coordinate system”, in which the shearing velocity of the plasma vanishes, and the two Maxwell equations and the Lorentz force on the particles are modified accordingly (see Riquelme et al. 2012).

Table 1
Shearing Simulation Parameters

Run	$\omega_{ce}^{\text{init}}/s$	N_{epc}	$d_e^{\text{init}}/\Delta_x$	L/R_{Le}^{init}	$c/[\Delta_x/\Delta_t]$
S300	300	100	35	140	0.225
S600	600	100	35	140	0.225
S1200	1200	100	35	140	0.225
S2400	2400	100	35	140	0.225
S1200a	1200	100	25	140	0.225
S1200b	1200	50	35	140	0.225
S1200c	1200	100	35	70	0.225

Note. Simulation parameters for the shearing runs: the electron magnetization $\omega_{ce}^{\text{init}}/s$, the number of macroelectrons per cell (N_{epc}), the initial electron skin depth $d_e^{\text{init}} (\equiv c/\omega_{pe}^{\text{init}})$ in terms of grid point spacing Δ_x , the box size in terms of the initial electron Larmor radius (L/R_{Le}^{init}), and the speed of light ($c/[\Delta_x/\Delta_t]$), where Δ_t is the simulation time step.

y-component of the mean field evolves as a function of time t as $\langle B_y \rangle = -sB_0t$ (throughout this paper, $\langle \rangle$ represents an average over the simulation domain), implying that $|\langle \mathbf{B} \rangle|$ grows as $|\langle \mathbf{B} \rangle| = B_0(1 + (st)^2)^{1/2}$. In the compressing case, $\mathbf{v} = -q(y\hat{y} + z\hat{z})/(1 + qt)$, where q is a constant that quantifies the compression rate of the simulation box. In this case, $|\langle \mathbf{B} \rangle| = B_0(1 + qt)^2$ (the compressing setup is shown in Figure 1 of Sironi & Narayan 2015).

The initial plasma parameters in our simulations are chosen so that they represent typical ALT conditions. In these environments, the reported electron temperatures are usually of a few tens of MK (Feldman et al. 1994; Masuda et al. 1994, 1995; Fletcher et al. 2011). Our simulations thus use an initial temperature of 52 MK, which, when normalized by the electron rest-mass energy, gives $\Theta_e^{\text{init}} \equiv k_B T_e^{\text{init}}/m_e c^2 = 0.00875$ (k_B is the Boltzmann constant, m_e is the electron mass, and c is the speed of light). Additionally, the magnetic field intensity, B , is typically close to ~ 100 G (Kuridze et al. 2019), while the electron density, n_e , is usually estimated in the range $\sim 10^8$ – 10^{12} cm^{-3} (Feldman et al. 1994; Masuda et al. 1994, 1995; Tsuneta et al. 1997). If we define the ratio

$$f_e \equiv \frac{\omega_{ce}}{\omega_{pe}}, \quad (1)$$

where ω_{ce} and ω_{pe} are the electron cyclotron and plasma frequencies, respectively, we find that when choosing the fiducial values $B \sim 100$ G and $n_e \sim 10^9$ cm^{-3} , f_e becomes ~ 1 ($\omega_{ce} = |e|B/m_e c$ and $\omega_{pe} = (4\pi n_e e^2/m_e)^{1/2}$, where e is the electron charge). Our runs thus use an initial $f_e \approx 0.53$ (implying an initial electron beta $\beta_e^{\text{init}} = 0.0625$, where $\beta_e \equiv 8\pi n_e k_B T_e/B^2$). We run both our shearing and compressing simulations until f_e has been amplified to $f_e \approx 2$. This allows us to compare the shearing and the compressing run under similar plasma conditions. This also allows us to emphasize the important role played by f_e in determining both the dominant unstable modes and the efficiency of the acceleration.

Another important physical parameter in our runs is the initial electron “magnetization”, defined as the ratio of the initial electron cyclotron frequency and either the shear rate ($\omega_{ce}^{\text{init}}/s$) or the compression rate ($\omega_{ce}^{\text{init}}/q$). Although the magnetizations in our runs are much higher than unity, for computational convenience, we chose them much lower than expected in real flare conditions. Thus, we ensure that our magnetizations are high enough to not affect our results

Table 2
Compressing Simulation Parameters

Run	$\omega_{ce}^{\text{init}}/q$	N_{epc}	$d_e^{\text{init}}/\Delta_x$	L/R_{Le}^{init}	$c/[\Delta_x/\Delta_t]$
C300	300	200	50	78	0.13
C600	600	200	50	78	0.13
C1200	1200	200	50	78	0.13
C2400	2400	200	50	78	0.13
C2400a	2400	200	40	78	0.13
C2400b	2400	100	50	78	0.13
C2400c	2400	200	50	39	0.13

Note. Same as Table 1, but for the compressing runs.

significantly by using $\omega_{ce}^{\text{init}}/s$ (and $\omega_{ce}^{\text{init}}/q$) = 300, 600, 1200, and 2400 to show that our results tend to converge as the magnetization grows.

The numerical parameters in our runs are the number of macro-electrons per cell (N_{epc}), the initial electron skin depth $d_e^{\text{init}} (\equiv c/\omega_{pe}^{\text{init}})$ in terms of the grid point spacing Δ_x , the initial box size L in terms of the initial electron Larmor radius $R_{Le}^{\text{init}} (\equiv v_{th,e}/\omega_{ce}^{\text{init}}$, where $v_{th,e}^2 = k_B T_e^{\text{init}}/m_e$), and the speed of light c in units of Δ_x/Δ_t , where Δ_t is the simulation time step. We ran a series of simulations to ensure that our choices for magnetization and for numerical parameters do not affect our results; these simulations are summarized in Tables 1 and 2 for the shearing and compressing runs, respectively.

3. Electron Temperature Anisotropy Regulation

Before describing the effect of unstable plasma modes in producing electron acceleration, in this section we describe the way in which these modes regulate the temperature anisotropy. Since this regulation is qualitatively similar in the shearing and compressing runs, our description is based on the shearing simulations.

3.1. Interplay between Magnetic Field Growth and Temperature Anisotropy Evolution

Figure 1(a) shows in solid green the linear growth of the y-component of the mean magnetic field $\langle \mathbf{B} \rangle$ in shearing simulation S1200 (see Table 1). The x -component remains constant at a value of B_0 and the z (out of plane) component is zero, as expected in our shearing setup. In Figure 1(b) we see that, due to the growth of $|\langle \mathbf{B} \rangle|$, the electron temperatures perpendicular and parallel to $\langle \mathbf{B} \rangle$, $\Theta_{e,\perp} (\equiv k_B T_{e,\perp}/m_e c^2$; solid black) and $\Theta_{e,\parallel} (\equiv k_B T_{e,\parallel}/m_e c^2$; solid red), grow and decrease, respectively, as expected from their initially adiabatic evolutions. Indeed, in the initial regime, $\Theta_{e,\perp}$ and $\Theta_{e,\parallel}$ evolve according to the adiabatic Chew–Goldberg–Low (CGL) equation of state (Chew et al. 1956), shown by the dashed black and dashed red lines, respectively.⁸ The departure from the CGL evolution at $t \cdot s \approx 1.4$ coincides with the rapid growth and saturation of $\delta \mathbf{B} (\equiv \mathbf{B} - \langle \mathbf{B} \rangle)$, as shown by the solid red line in Figure 1(a). This shows that the growth of the temperature anisotropy is ultimately limited by temperature-anisotropy-unstable modes, which can break the adiabatic evolution of the electron temperatures by providing efficient pitch-angle scattering.

⁸ The CGL equation of state implies that $T_{e,\perp}/B$ and $T_{e,\parallel}\beta^2/n_e^2$ remain constant.

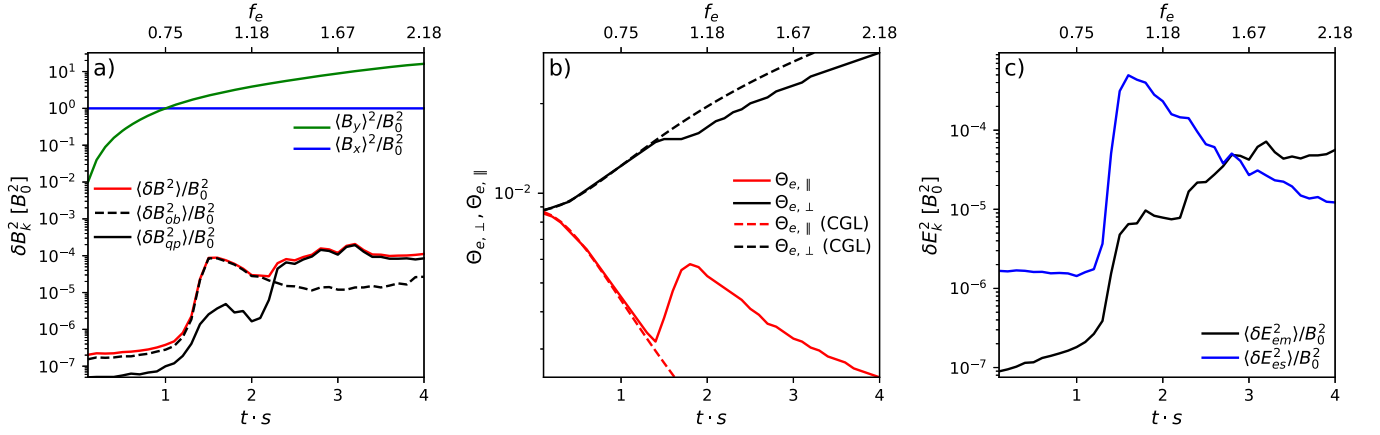


Figure 1. Fields and electron temperature evolutions for run S1200 as a function of time t in units of s^{-1} (lower horizontal axes) and of the instantaneous f_e (upper horizontal axes; using the average magnetic field at each time). Panel (a) shows in solid blue and solid green lines the evolution of the energy in the x and y components of the mean magnetic field $\langle \mathbf{B} \rangle$, respectively. The solid red line shows the energy in $\delta \mathbf{B}$, while the solid black (dashed black) line shows the contribution to the $\delta \mathbf{B}$ energy given by the quasiparallel (oblique) modes (all in units of the initial magnetic energy). Panel (b) shows in solid black (solid red) the evolution of the electron temperature perpendicular (parallel) to $\langle \mathbf{B} \rangle$. The dashed black (dashed red) line shows the CGL prediction for the perpendicular (parallel) temperature. Panel (c) shows in black (blue) the energy in the electromagnetic and electrostatic component of the electric field fluctuations $\delta \mathbf{E}$, which satisfy $\nabla \cdot \delta \mathbf{E} = 0$ and $\nabla \times \delta \mathbf{E} = 0$, respectively.

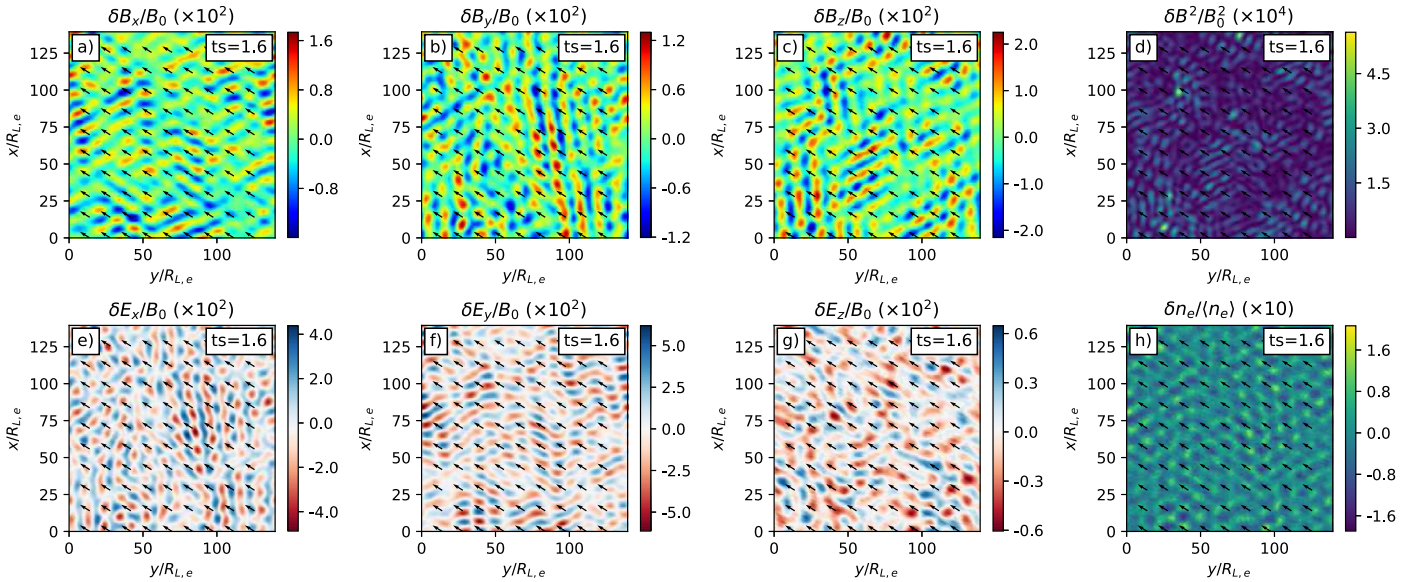


Figure 2. For run S1200, we show the 2D distribution of the three components of $\delta \mathbf{B}$: δB_x , δB_y , and δB_z , the three components of $\delta \mathbf{E}$: δE_x , δE_y , and δE_z , the total $\delta \mathbf{B}$ energy, and the electron density fluctuations δn_e ($\equiv n_e - \langle n_e \rangle$) at $t \cdot s = 1.6$. Fields and density are normalized by B_0 and by the average density $\langle n_e \rangle$, respectively. The black arrows show the direction of the average magnetic field $\langle \mathbf{B} \rangle$.

3.2. The Nature of the Unstable Modes

A 2D view of the relevant unstable modes at $t \cdot s = 1.6$ (right after the saturation of $\delta \mathbf{B}$) is given by Figure 2, which shows the three components of the magnetic and electric fluctuations $\delta \mathbf{B}$ and $\delta \mathbf{E}$.⁹ Both the magnetic and electric fluctuations show that the dominant modes have an oblique wavevector with respect to the direction of the mean magnetic field $\langle \mathbf{B} \rangle$, which is shown by the black arrows in all the panels. The dominance of the oblique modes stops at a later time, as can be seen from Figure 3, which shows the same quantities as Figure 2, but at $t \cdot s = 3.1$. In this case, the waves propagate along the background magnetic field, implying that quasiparallel modes dominate both the electric and magnetic fluctuations.

In order to determine the transition time from the dominance of oblique to quasiparallel modes, we calculate the magnetic energy contained in each type of modes. For this, we define the modes as “oblique” or “quasiparallel” depending on whether the angle between their wavevector \mathbf{k} and $\langle \mathbf{B} \rangle$ is larger or smaller than 20° , respectively. The magnetic energies in oblique and quasiparallel modes are shown in Figure 1(a) using dashed black and solid black lines and are denoted by $\langle \delta B_{ob}^2 \rangle$ and $\langle \delta B_{qp}^2 \rangle$, respectively. We see that the oblique modes dominate until $t \cdot s \approx 2.2$. After that, the quasiparallel modes contribute most of the energy of the magnetic fluctuations, which is consistent with the two regimes shown in Figures 2 and 3.

An interesting characteristic of the oblique modes is the notorious fluctuations in the electron density n_e , as shown in Figure 2(h), which suggest the presence of a significant electrostatic component in the electric field $\delta \mathbf{E}$. These density fluctuations are less prominent in the case that is dominated by

⁹ $\delta \mathbf{E}$ is simply equal to \mathbf{E} because $\langle \mathbf{E} \rangle = 0$ in our shearing coordinate setup.

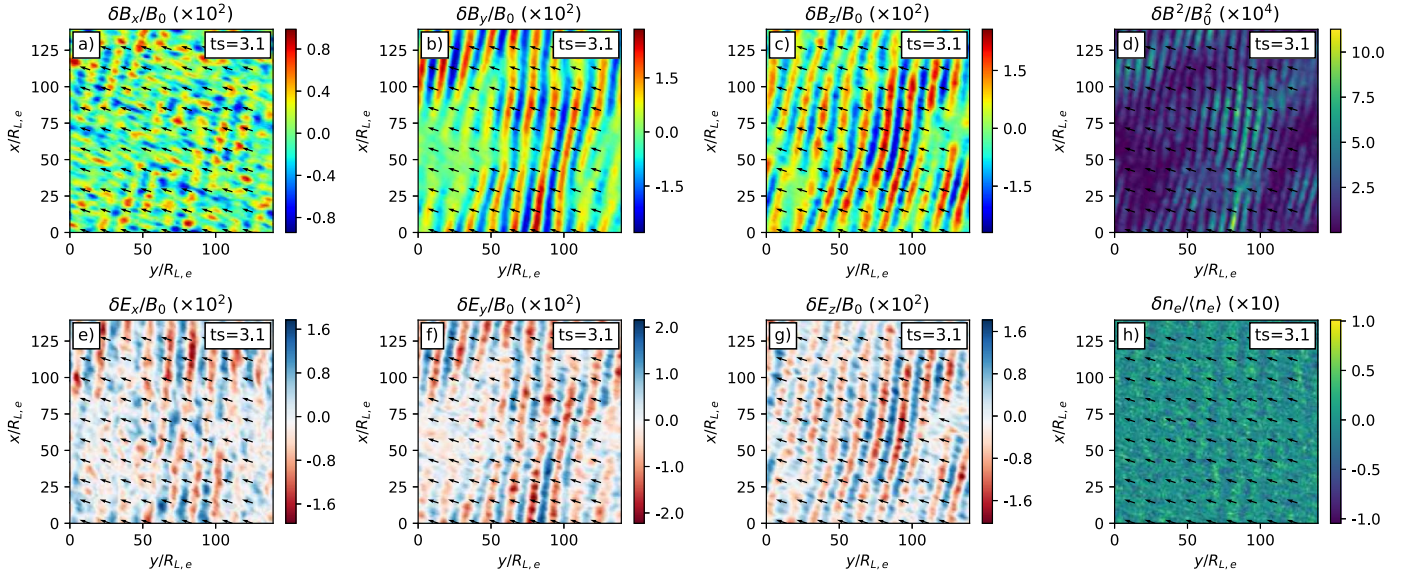


Figure 3. Same as Figure 2, but at $t \cdot s = 3.1$.

quasiparallel modes, as can be seen from Figure 3(h), which shows that at $t \cdot s = 3.1$, the electrostatic electric fields are weaker than at $t \cdot s = 1.6$. This change in the δE behavior can be seen more clearly in Figure 1(c), which shows the evolution of the energy contained in the electric field fluctuations δE , dividing it into its electrostatic and electromagnetic components (blue and black lines, respectively). This separation is achieved by distinguishing the contributions to the Fourier transform of the electric field fluctuations ($\delta \vec{E}$) that satisfy $\mathbf{k} \times \delta \vec{E} = 0$ (electrostatic part) and $\mathbf{k} \cdot \delta \vec{E} = 0$ (electromagnetic part). In the oblique regime ($t \cdot s \lesssim 2.2$), the electric field energy is mainly dominated by its electrostatic part (δE_{cs}^2), and after this, it gradually becomes dominated by its electromagnetic part (δE_{em}^2). Figure 1(c) also shows that this transition occurs when the instantaneous parameter f_e (shown by the upper horizontal axis) is $f_e \sim 1.2$ – 1.5 . We see in the next section that this transition is fairly consistent with linear Vlasov theory.

3.3. Comparison with Linear Vlasov Theory

In this section, we show that the transition from the dominance of oblique modes with a mainly electrostatic electric field (hereafter, oblique electrostatic modes) to the dominance of quasiparallel modes with a mainly electromagnetic electric field (hereafter, quasiparallel electromagnetic modes) in S1200 is consistent with linear Vlasov theory. Indeed, a previous study by Gary & Cairns (1999) predicts that for the range of electron conditions considered in our study and assuming a bi-Maxwellian electron velocity distribution, three types of modes are relevant: parallel, electromagnetic whistler (PEMW) modes; parallel, electromagnetic z (PEMZ) modes; and oblique, quasi-electrostatic (OQES) modes, where the latter are dominated by electrostatic electric fields. In this section we use linear Vlasov theory to check whether the PEMW or PEMZ (OQES) modes are theoretically the most unstable when the quasiparallel electromagnetic (oblique electrostatic) modes dominate in our run. For this we use the NHDS solver of Verscharen & Chandran (2018) to calculate the temperature anisotropy threshold $\Theta_{e,\perp}/\Theta_{e,\parallel} - 1$ needed for the growth of these modes, with a given growth rate γ_g , assuming different values of f_e and $\Theta_{e,\parallel}$.

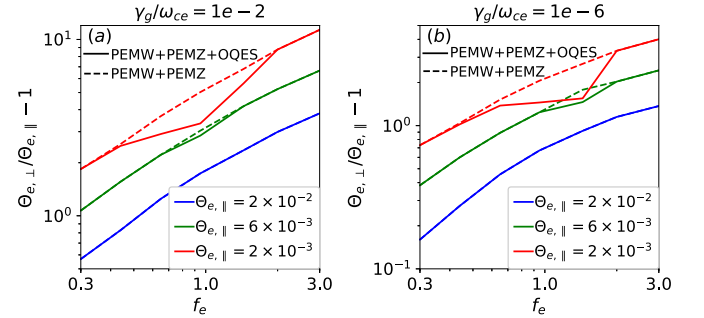


Figure 4. The anisotropy thresholds $\Theta_{e,\perp}/\Theta_{e,\parallel} - 1$ for the growth of parallel, electromagnetic PEMW and PEMZ modes (dashed lines) and of the combination of PEMW and PEMZ modes in addition to OQES modes (solid lines) as a function of f_e and for $\Theta_{e,\parallel} = 0.002$ (red), 0.006 (green), and 0.02 (black). Calculations were performed using the NHDS solver of Verscharen & Chandran (2018). Panels (a) and (b) show the cases with growth rates $\gamma_g = 10^{-2} \omega_{ce}$ and $\gamma_g = 10^{-6} \omega_{ce}$, respectively.

Figure 4(a) shows the anisotropy thresholds for $\gamma_g/\omega_{ce} = 10^{-2}$, which is appropriate for run S1200. We estimate the growth rate of δB in this run from its exponential growth regime in Figure 1(a) ($t \cdot s \sim 1.2$ – 1.3), which is $\gamma_g \sim 10$. This implies that $\gamma_g \sim 10^{-2} \omega_{ce}^{\text{init}}$, given that in run S1200, $\omega_{ce}^{\text{init}}/s = 1200$. The dashed lines in Figure 4(a) consider the thresholds only for parallel modes (i.e., they consider the lowest threshold between PEMW and PEMZ modes), while the solid lines consider the lowest threshold between modes with all propagation angles. We find that for $\Theta_{e,\parallel} = 0.002$ and 0.006 , there are values of f_e where the solid red and solid green lines separate from the corresponding dashed lines. These values of f_e therefore correspond to where the unstable modes are dominated by OQES modes, which for $\Theta_{e,\parallel} = 0.002$ and 0.006 occurs when $0.4 \lesssim f_e \lesssim 1.8$ and $0.8 \lesssim f_e \lesssim 1.3$, respectively. For values of f_e above and below these ranges, linear theory predicts that the most unstable modes correspond to PEMZ and PEMW modes, respectively, which is consistent with the merging of the dashed and solid lines in these regimes.¹⁰

¹⁰ The predictions shown in Figure 4(a) are in good agreement with Figure 4(c) of Gary & Cairns (1999).

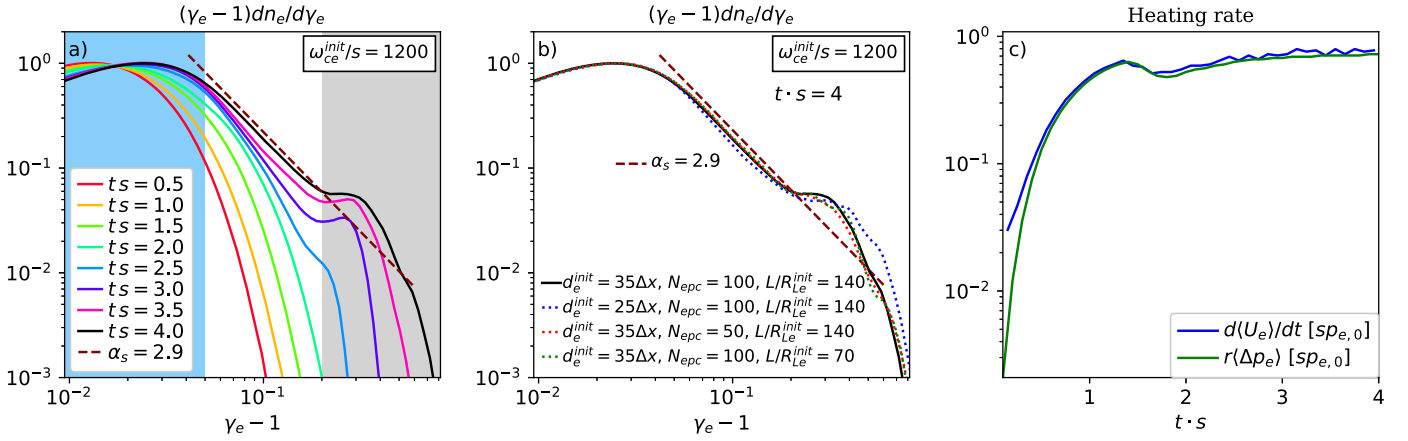


Figure 5. (a) The electron energy spectrum for run S1200 for different values of $t \cdot s$, where γ_e is the Lorentz factor of the electrons. The dashed brown line shows a power law of index $\alpha_s \approx 2.9$, which resembles part of the final nonthermal tail. (b) Test of numerical convergence of the final spectrum. We show the electron energy spectra at $t \cdot s = 4$ for runs analogous to S1200 (solid black), but using (i) a lower time and space resolution $d_e^{\text{init}}/\Delta x = 25$ (run S1200a, dotted blue line), (ii) a smaller $N_{\text{epc}} = 50$ (run S1200b, dotted red line), and (iii) a smaller box size $L/R_{Le}^{\text{init}} = 70$ (run S1200c, dotted green line). No significant difference can be seen between the different spectra. (c) The time evolution of $d\langle U_e \rangle/dt$ (blue) and of $r\langle \Delta p_e \rangle$ (green) for the same run, normalized by $sp_{e,0}$, where $p_{e,0}$ is the initial electron pressure.

Thus, the dominance of oblique electrostatic modes in run S1200 from the moment when the instability sets in ($f_e \sim 0.8$) until $f_e \sim 1.2$ – 1.5 , suggests that, in order to be consistent with linear theory, $\Theta_{e,\parallel}$ should be in the range ~ 0.002 – 0.006 after the growth of the instabilities ($f_e \gtrsim 0.8$). This is indeed what is shown by Figure 1(b), where $\Theta_{e,\parallel}$ (solid red line) appears in the range $\Theta_{e,\parallel} \sim 0.0025$ – 0.005 when $f_e \gtrsim 0.8$.

These results show that the transition between the oblique, electrostatic to quasiparallel, electromagnetic regimes at $f_e \sim 1.2$ – 1.5 in run S1200 is consistent with linear Vlasov theory, which predicts a transition from OQES to PEMZ modes at $f_e \sim 1.3$ – 1.8 . Therefore, hereafter we refer to the $f_e \lesssim 1.2$ – 1.5 and $f_e \gtrsim 1.2$ – 1.5 regimes as OQES-dominated and PEMZ-dominated regimes, respectively.

4. Electron Nonthermal Acceleration

Previous works show that pitch-angle scattering by temperature anisotropy instabilities can produce significant stochastic particle acceleration (Riquelme et al. 2017; Ley et al. 2019). In this section we show that electron temperature anisotropy instabilities can also contribute significantly to the acceleration of electrons under the conditions expected in contracting loop tops in solar flares, which are defined by the magnetic field strength and the electron density and temperature. We show this first for the $\omega_{ce}^{\text{init}}/s = 1200$ run S1200, and then we show that the acceleration is fairly independent of $\omega_{ce}^{\text{init}}/s$.

4.1. Case $\omega_{ce}^{\text{init}}/s = 1200$

The electron energy spectrum evolution for run S1200 can be seen from Figure 5(a), which shows $dn_e/d\ln(\gamma_e - 1)$ for different values of $t \cdot s$ (γ_e is the electron Lorentz factor). This plot shows the rapid growth of a nonthermal tail starting at $t \cdot s \approx 2.5$. After $t \cdot s \approx 3.5$, this tail can be approximated as a power law of index $\alpha_s \approx 2.9$ ($\alpha_s \equiv d\ln(n_e)/d\ln(\gamma_e - 1)$), plus a high-energy bump that reaches $\gamma_e - 1 \sim 0.6$ (~ 300 keV). Most of the nonthermal behavior of the spectrum starts at $t \cdot s \approx 2.5$, which is right after the quasiparallel electromagnetic modes become dominant, as shown by Figure 1(c).

Figure 5(b) shows a numerical convergence test of the final spectrum at $t \cdot s = 4$. It compares run S1200 ($d_e^{\text{init}}/\Delta x = 35$,

$N_{\text{epc}} = 100$, and $L/R_{Le}^{\text{init}} = 140$) with a run with $d_e^{\text{init}}/\Delta x = 25$ (run S1200a, dotted blue line), a run with $N_{\text{epc}} = 50$ (run S1200b, dotted red line), and a run with $L/R_{Le}^{\text{init}} = 70$ (run S1200c, dotted green line). No significant difference can be seen between the different spectra, implying that our results are fairly converged numerically.

In order to identify the energy source for the nonthermal electron acceleration, we explore first the overall energy source for electrons (thermal and nonthermal). It is well known that the presence of a temperature anisotropy in a shearing, collisionless plasma gives rise to particle heating due to the so-called ‘‘anisotropic viscosity’’ (AV). This viscosity can give rise to an overall electron heating, for which the time derivative of the electron internal energy, U_e , is (Kulsrud 1983; Snyder et al. 1997)

$$\frac{dU_e}{dt} = r\Delta p_e, \quad (2)$$

where r is the growth rate of the field (in our setup, $r = -sB_x B_y/B^2$) and Δp_e is the difference between the perpendicular and parallel electron pressures, $\Delta p_e = p_{e,\perp} - p_{e,\parallel}$. In run S1200, Equation (2) reproduces the evolution of the overall electron energy gain well. This can be seen from Figure 5(c), where the time derivative of the average electron internal energy $d\langle U_e \rangle/dt$ (blue) coincides well with $r\langle \Delta p_e \rangle$ (green). This result shows that in our shearing setup, the heating by AV essentially explains all of the electron energization.

Although the total electron energy gain is dominated by AV, the work done by the electric field $\delta\vec{E}$ associated with the unstable modes, $W_E (\equiv \int e\delta\vec{E} \cdot d\vec{r}$, where \vec{r} is the electron position), can differ significantly between electrons from different parts of the spectrum, making W_E play a key role in producing the nonthermal tail by transferring energy from the thermal to the nonthermal part of the spectrum (Riquelme et al. 2017; Ley et al. 2019). We check this by analyzing the contributions of AV and W_E to the energy gain of three different electron populations, defined by their final energy at $t \cdot s = 4$. These populations are listed below.

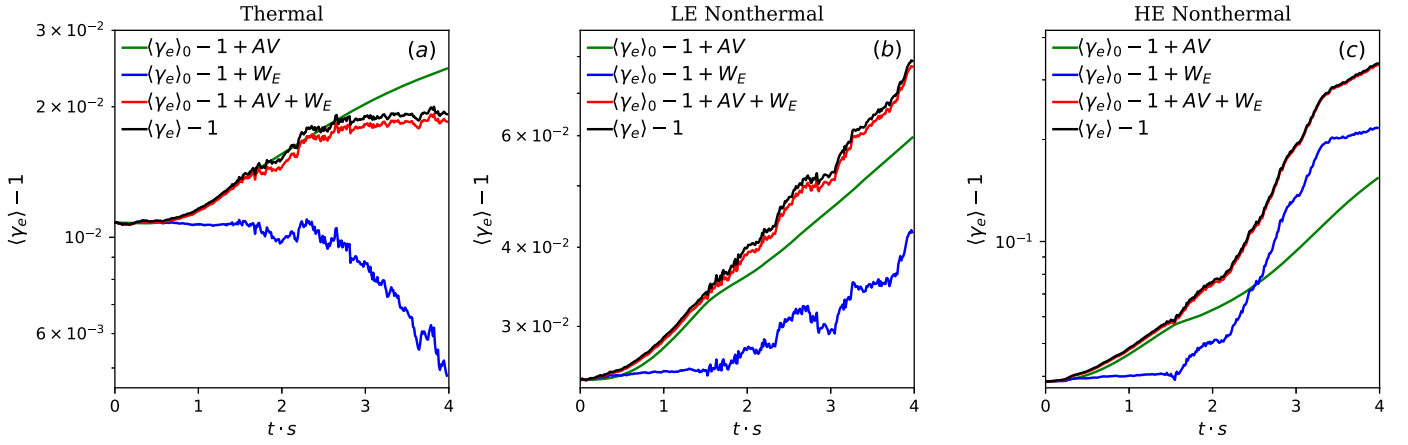


Figure 6. The different contributions to electron energization for three electron populations in run S1200, normalized by m_{ec}^2 . Panel (a) shows the case of the thermal electrons, defined by their final ($t \cdot s = 4$) Lorentz factor being $\gamma_e - 1 < 0.05$ (marked by the light blue region of Figure 5(a)). Panels (b) and (c) show the low-energy and high-energy nonthermal electrons, defined by their final Lorentz factor being in the ranges $0.05 < \gamma_e - 1 < 0.2$ and $0.2 < \gamma_e - 1$, respectively (marked by the white and gray regions in Figure 5(a), respectively). In all three panels, the black line shows the energy evolution of the electrons. The green line shows their average energy gain due to AV. The blue lines shows the same, but considering the energization by the electric field of the unstable modes (W_E) instead of the energization by AV. The red line shows the energy gain by the addition of AV and W_E , and reproduces the total energy evolutions shown as black lines reasonably well.

1. *Thermal electrons*: their final energy satisfies $\gamma_e - 1 < 0.05$, which corresponds to the energy range marked by the light blue background in Figure 5(a).
2. *Low-energy nonthermal electrons*: their final energies satisfy $0.05 < \gamma_e - 1 < 0.2$, where the nonthermal tail roughly behaves as a power law of index $\alpha_s \approx 2.9$. This energy range is marked by the white background in Figure 5(a).
3. *High-energy nonthermal electrons*: corresponding to the high-energy bump in the spectrum, defined by $0.2 < \gamma_e - 1$. This energy range is marked by the gray background in Figure 5(a).

Figures 6(a), 6(b), and 6(c) show the energy evolution for the thermal, low-energy nonthermal, and high-energy nonthermal electrons, respectively. In each case, we show the average initial kinetic energy of each population, $\langle \gamma_e \rangle_0 - 1$, plus

1. the work done by the electric field of the unstable modes, W_E , shown by the blue lines,
2. the energy gain by the anisotropic viscosity, AV, shown by the green lines,
3. the total energy gain, shown by the black lines.

The green lines show that for the three populations, there is a positive energy gain due to AV. On the other hand, the blue lines in Figure 6(a) show that, in the case of the thermal electrons, W_E produces a decrease in the electron energies. This illustrates that the thermal electrons transfer a significant part ($\sim 50\%$) of their initial energy to the unstable modes. However, the overall heating of the thermal electrons is positive and, by the end of the simulation, reaches an increase of a factor ~ 2 in their thermal energy. Figures 6(b) and 6(c) show that for the low- and high-energy nonthermal electrons, there is a significant growth in the electron energy due to W_E , suggesting that the unstable modes transfer energy to the nonthermal particles. For the low-energy nonthermal electrons, the AV still dominates the heating, whereas for the high-energy nonthermal electrons, AV is subdominant and most of the electron energization is due to W_E . The red lines in Figures 6(a), 6(b), and 6(c) show the overall heating of thermal electrons due to adding AV and W_E . The red line reproduces the evolution of

the total energy $\langle \gamma_e \rangle - 1$ (black line) of the three electron populations reasonably well.

The way AV and W_E contribute to the energization of thermal and nonthermal electrons suggests that the formation of an electron nonthermal tail is caused by the transfer of energy from the thermal to the nonthermal electrons, which is mediated by the electric field of the waves. This characteristic of the formation of a nonthermal tail is in line with previous results, where the acceleration of ions and electrons by temperature anisotropy instabilities was studied in nearly relativistic plasmas (Riquelme et al. 2017; Ley et al. 2019). Also, Figures 6(a), 6(b), and 6(c) show that most of the energy transfer from thermal to nonthermal electrons occurs after $t \cdot s \sim 2.2$, which corresponds to the regime dominated by PEMZ modes, implying a subdominant contribution to the acceleration by the initially dominant OQES modes.

4.2. Extrapolation to the (Realistic) Very High ω_{ce}/s Regime

The shear parameter s is a measure of the rate at which temperature anisotropy growth is driven in our simulations. We can thus estimate the corresponding parameter s in the contracting loop tops of solar flares as the rate at which temperature anisotropy grows in these environments. This can be obtained by estimating the inverse of the time that it takes for the contracting loop tops to collapse into a more stable configuration.

We thus estimate s by dividing the typical Alfvén velocity, v_A , in the loop tops (v_A should be close to the speed at which the newly reconnected loops are ejected from their current sheet) by the typical length scale of the contracting loop tops, L_{LT} . Using our fiducial parameters $n_e \sim 10^9 \text{ cm}^{-3}$ and $B \sim 100 \text{ G}$, and estimating $L_{LT} \sim 10^9 \text{ cm}$ (e.g., Chen et al. 2020), we obtain $s \sim 1 \text{ s}^{-1}$ and $\omega_{ce}/s \sim 10^9$. This value of ω_{ce}/s is several orders of magnitude higher than what can be achieved in our simulations. Therefore, two important questions arise. The first question is whether for realistic values of ω_{ce}/s , the dominance of PEMZ and OQES modes should occur for the same regimes as observed in run S1200. And, if that is the case, the second question is whether the effect on electron acceleration of these modes remains the same, independently of ω_{ce}/s .

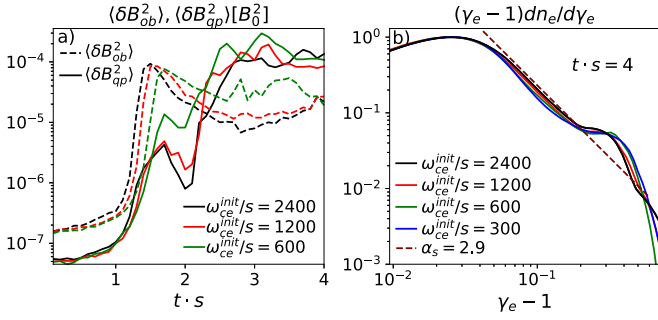


Figure 7. (a) The evolution of the energy in δB divided into oblique (dashed) and quasiparallel (solid) modes for runs S2400 (black), S1200 (red), and S600 (green). These runs are equal except for having $\omega_{ce}^{init}/s = 2400, 1200,$ and 600 , respectively. (b) The final electron spectra for runs S2400 (black), S1200 (red), S600 (green), and S300 (blue).

Since in Section 3.3 we showed that linear Vlasov theory is suitable for predicting the dominance of the different modes, in this section, we use linear theory to show that increasing ω_{ce}^{init}/s by several orders of magnitude should not modify the relative importance of the modes in the different plasma regimes. First, we note that the growth rate γ_g of the unstable modes should be proportional to s , implying that $\omega_{ce}^{init}/s \propto \omega_{ce}^{init}/\gamma_g$. This proportionality is physically expected because s^{-1} sets the timescale for the evolution of the macroscopic plasma conditions. Thus, the different modes that dominate in different simulation stages need to have a growth rate of about s to have time to set in and regulate the electron temperature anisotropy. This can also be seen from Figure 7(a), which shows the evolution of the energy in δB divided into oblique and quasiparallel modes (dashed and solid lines, respectively) for runs with $\omega_{ce}^{init}/s = 600, 1200,$ and 2400 (runs S600, S1200, and S2400, respectively). We see that the three runs show essentially the same ratio $\gamma_g/s \sim 10$. This means that, in order to find out which instabilities would dominate for realistically high values of ω_{ce}^{init}/s , we must calculate the instability thresholds for a comparatively high value of ω_{ce}/γ_g . Following this criterion, Figure 4(b) shows these thresholds using the same values of f_e and $\Theta_{e,\parallel}$ as were used in Figure 4(a), but assuming $\gamma_g/\omega_{ce} = 10^{-6}$ instead of 10^{-2} . We see that for $\gamma_g/\omega_{ce} = 10^{-6}$, the PEMW, PEMZ, and OQES modes dominate for values of f_e and $\Theta_{e,\parallel}$ that are very similar to those shown for $\gamma_g/\omega_{ce} = 10^{-2}$. This implies that the role played by the different modes in controlling the electron temperature anisotropy in the different plasma regimes should not change significantly for realistic values of the shearing parameter s .

We now investigate whether increasing ω_{ce}^{init}/s affects the spectral evolution of the electrons. This is done in Figure 7(b), where the final spectra ($t \cdot s = 4$) are shown for runs with $\omega_{ce}^{init}/s = 300, 600, 1200,$ and 2400 (runs S300, S600, S1200, and S2400, respectively). No significant differences are seen in the final spectra, except for a slight hardening as ω_{ce}^{init}/s increases, which does not seem significant when comparing the cases $\omega_{ce}^{init}/s = 2400$ and 1200 . This shows that the magnetization parameter ω_{ce}^{init}/s does not play a significant role in the efficiency of the electron nonthermal acceleration.

The lack of a dependence of the acceleration on ω_{ce}^{init}/s can be physically understood in terms of the relation between the effective pitch-angle scattering rate due to the instabilities, ν_{eff} , and s . We estimate ν_{eff} using the evolution of $\Theta_{e,\parallel}$, which in a

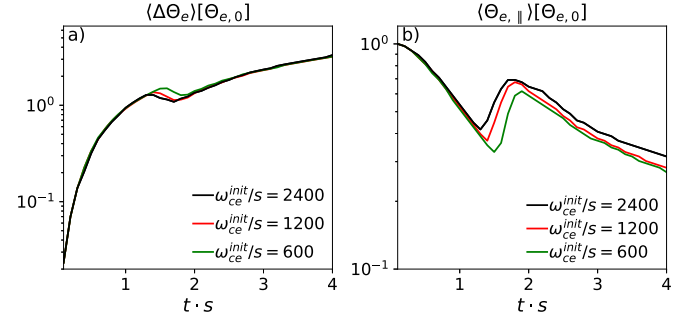


Figure 8. (a) The evolution of the average $\Delta \Theta_e$ for runs S2400 (black), S1200 (red), and S600 (green). (b) The evolution of the average $\Theta_{e,\parallel}$ for the same runs.

slowly evolving and homogeneous shearing plasma is given by Sharma et al. (2007),

$$\frac{d\Theta_{e,\parallel}}{dt} + 2\Theta_{e,\parallel}\hat{\mathbf{b}}\hat{\mathbf{b}} : \nabla \mathbf{v} = \nu_{eff} \frac{2}{3} \Delta \Theta_e, \quad (3)$$

where \mathbf{v} is the plasma shear velocity, $\hat{\mathbf{b}} = \hat{\mathbf{B}}/B$, and $\Delta \Theta_e = \Theta_{e,\perp} - \Theta_{e,\parallel}$. Considering that $\mathbf{v} = -sx\hat{\mathbf{y}}$, we can rewrite Equation (3) as

$$\frac{d\Theta_{e,\parallel}}{d(ts)} + 2\Theta_{e,\parallel}\hat{b}_x\hat{b}_y = \frac{2}{3} \Delta \Theta_e \frac{\nu_{eff}}{s}. \quad (4)$$

Figure 8(a) shows the evolution of $\langle \Delta \Theta_e \rangle$ for the runs with $\omega_{ce}^{init}/s = 600, 1200,$ and 2400 (runs S600, S1200, and S2400). When $t \cdot s \gtrsim 2.2$, the factor $\Delta \Theta_e$ that appears on the right-hand side of Equation (4) is very similar in the three runs. The left-hand side of Equation (4) depends on the evolution of $\Theta_{e,\parallel}$, which in the $t \cdot s \gtrsim 2.2$ regime is also similar in the three runs, as can be seen from Figure 8(b). This means that for $t \cdot s \gtrsim 2.2$, the ratio ν_{eff}/s in Equation (4) is fairly constant (within about $\sim 10\%$) for these three values of ω_{ce}^{init}/s . Thus, for simulations with a fixed value of ω_{ce}^{init} but different s , the behaviors of $\langle \Delta \Theta_e \rangle$ and $\langle \Theta_{e,\parallel} \rangle$ for $t \cdot s \gtrsim 2.2$ imply that ν_{eff} should be approximately proportional to s . Because of this, the number of times that the electrons are strongly deflected in a fixed interval of $t \cdot s$ should be largely independent of ω_{ce}^{init}/s on average. Thus, in a stochastic acceleration scenario, we expect the acceleration effect during a fixed number of shear times (s^{-1}) to only depend on the dispersive properties of the unstable modes (see, e.g., Summers et al. 1998), which are not expected to depend on the value of ω_{ce}^{init}/s . Indeed, as long as $\omega_{ce}^{init} \gg s$, the mode propagation and oscillations should occur rapidly (on timescales of $\sim \omega_{ce}^{-1}$), and should not be affected by the slowly evolving background (on timescales of $\sim s^{-1}$). These arguments thus imply that the acceleration efficiency should be largely independent of ω_{ce}^{init}/s .

We note that Figures 8(a) and 8(b) show that in the $t \cdot s \lesssim 2.2$ regime, $\langle \Delta \Theta_e \rangle$ and $\langle \Theta_{e,\parallel} \rangle$ tend to depend more strongly on ω_{ce}^{init}/s , so the electron acceleration efficiency should differ significantly during this period. However, Figure 7(a) shows that for $t \cdot s \lesssim 2.2$, the dominant instabilities are mainly oblique modes, which is indicative of the dominance of OQES modes. Therefore, since no significant acceleration is expected to happen in that regime (as we showed in Section 4.1), the different evolutions of $\langle \Delta \Theta_e \rangle$ and $\langle \Theta_{e,\parallel} \rangle$ for $t \cdot s \lesssim 2.2$ should

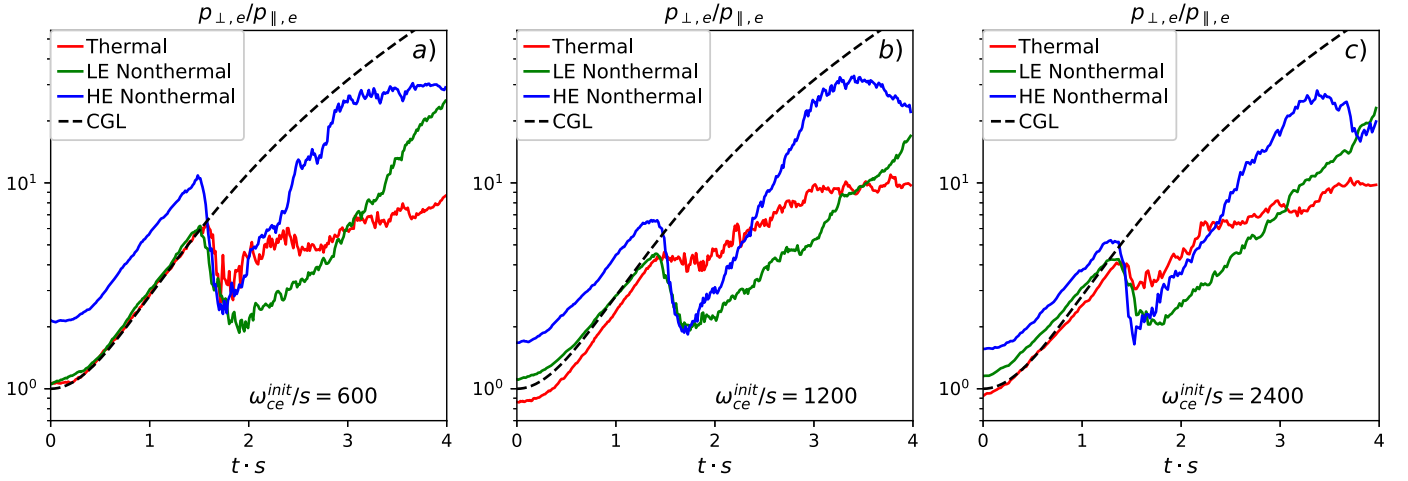


Figure 9. Panels (a), (b), and (c) show $p_{e,\perp}/p_{e,\parallel}$ for different populations in runs with $\omega_{ce}^{\text{init}}/s = 600, 1200,$ and $2400,$ respectively (runs S600, S1200, and S2400, respectively). The populations correspond to the thermal (red), low-energy nonthermal (green), and high-energy nonthermal (blue) electrons, which are defined in Section 4.1 according to their final energies. In the three panels we also show as dashed black lines the estimated CGL evolution of $p_{e,\perp}/p_{e,\parallel}$ for an initially isotropic population.

not have an appreciable effect on the final electron spectra. Although this analysis is valid for the rather limited range of values of $\omega_{ce}^{\text{init}}/s$ tested by our simulations, we expect the $\nu_{\text{eff}} \propto s$ relation to hold even for realistic values of $\omega_{ce}^{\text{init}}/s$. This is based on comparing the linear theory thresholds presented in Figures 4(a) and 4(b), which predict $\Delta\Theta_e/\Theta_{e,\parallel}$ to have essentially the same evolution (only differing by an overall factor ~ 3) when decreasing γ_g/ω_{ce} by four orders of magnitude.

4.3. Pitch-angle Evolution

The evolution of the electron pitch angle is important to determine the ability of the electrons to escape the flare loop tops and precipitate toward the footpoints, which is a key ingredient for solar flare emission models (e.g., Minoshima et al. 2011). In this section we investigate the way temperature anisotropy instabilities affect the pitch-angle evolution for electrons with different energies.

As a measure of the average pitch angle for different electron populations, Figure 9(b) shows $p_{e,\perp}/p_{e,\parallel}$ for the thermal (red), low-energy nonthermal (green), and high-energy nonthermal (blue) electrons from run S1200. These three electron populations are defined according to their final energies, as we did in Section 4.1 (in each of these cases, the pressures are calculated only considering the electrons in each population). For comparison, we also show as dashed black lines the time dependence of $p_{e,\perp}/p_{e,\parallel}$ for a hypothetical, initially isotropic electron population that evolves according to the CGL equation of state. The three electron populations show evolutions similar to the CGL prediction until the onset of the OQES instability, which, as we saw in Section 3, occurs at $t \cdot s \sim 1.4$. After this, the pitch-angle scattering tends to reduce $p_{e,\perp}/p_{e,\parallel}$ for the three populations, which occurs more abruptly for the low- and high-energy nonthermal electrons, whose pitch angles by $t \cdot s \sim 1.7$ become ~ 2 – 3 times smaller than those of the thermal electrons. This shows that even though the OQES modes (which dominate until $t \cdot s \approx 2.2$) make a subdominant contribution to the nonthermal electron acceleration, they still have an important effect by significantly reducing the pitch angle of the highest energy particles. After this, in the PEMZ-dominated regime, the anisotropy evolves in the opposite way. In this case,

the $p_{e,\perp}/p_{e,\parallel}$ ratios of both populations of nonthermal electrons grow more rapidly than for the thermal electrons. This is especially true for the high-energy nonthermal electrons, for which $p_{e,\perp}/p_{e,\parallel}$ reaches values ~ 2 – 3 times higher than for thermal electrons by the end of the run.

This increase in the electron pitch angle of the highest energy electrons due to PEMZ-mode scattering is consistent with quasilinear theory results that describe the stochastic acceleration of electrons by whistler/z modes in terms of the formation of a “pancake” pitch-angle distribution for the most accelerated electrons (Summers et al. 1998). These results thus suggest that, assuming a more realistic solar flare scenario where the electrons were allowed to precipitate toward the flare footpoints, the high-energy nonthermal electrons produced by PEMZ-mode scattering should tend to be more confined to the loop top than the low-energy nonthermal and thermal electrons.

Figures 9(a) and 9(c) show the same quantities as Figure 9(b), but for runs with $\omega_{ce}^{\text{init}}/s = 600$ and 2400 (runs S600 and S2400). After the triggering of the instabilities ($t \cdot s \sim 1.4$), there are no substantial differences between the three magnetizations, suggesting that the energy dependence of the pitch-angle evolution in our runs is fairly independent of $\omega_{ce}^{\text{init}}/s$.

4.4. Role of the Initial Conditions in the Final Electron Energies

An interesting aspect of the electron energy evolution is the correlation between the final electron energies and (i) their initial energies and (ii) their initial pitch angles. The correlation between the initial and final energies can be seen from Figures 6(a), 6(b), and 6(c), which show that for the thermal, low-energy nonthermal, and high-energy nonthermal electrons, the initial energies are given by $\langle \gamma_e \rangle_0 - 1 \sim 0.01, \sim 0.025,$ and $\sim 0.04,$ respectively. This energy correlation is also expected from the quasilinear theory results of Summers et al. (1998), which show that the maximum energy that electrons can acquire due to stochastic acceleration by whistler/z modes increases for higher initial energies (assuming a fixed value of f_e).

Additionally, Figure 9(b) shows that the initial values of $p_{e,\perp}/p_{e,\parallel}$ are higher for electrons that end up being more energetic, with the initial $p_{e,\perp}/p_{e,\parallel}$ being $\sim 0.9, \sim 1.1,$ and ~ 1.7 for the thermal, low-energy nonthermal, and high-energy

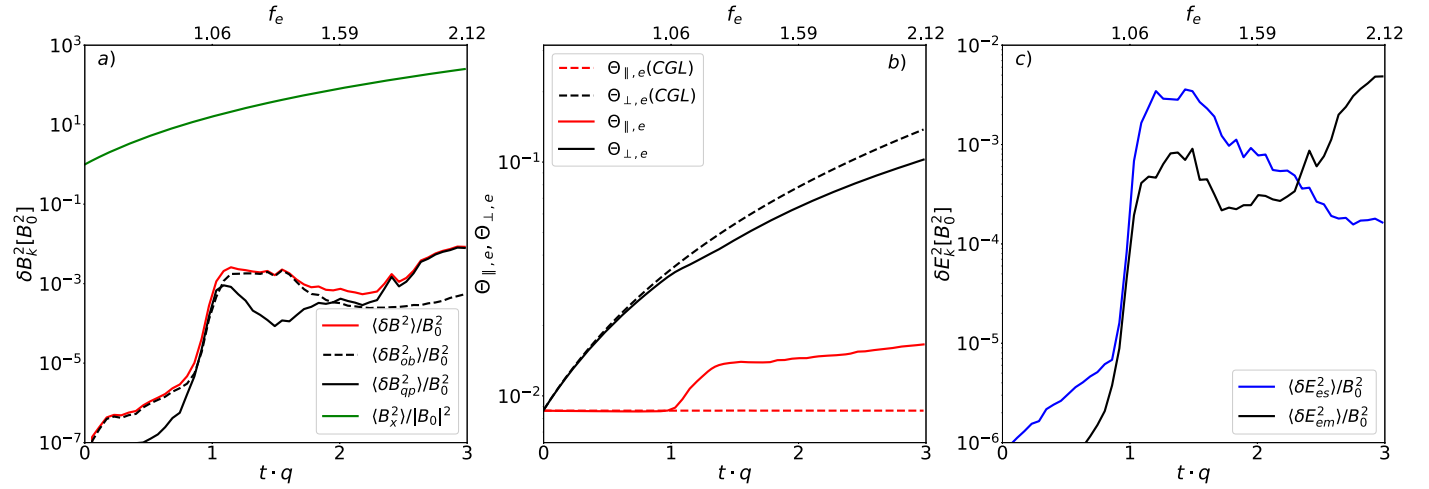


Figure 10. We show fields and electron temperature evolutions for the compressing run C2400 ($\omega_{ce}^{\text{init}}/q = 2400$) as a function of time tq and of the instantaneous f_e . (a) The solid green line shows the evolution of the energy in the x -component of $\langle \mathbf{B} \rangle$. The solid red line shows the energy in $\delta \mathbf{B}$, while the solid black (dashed black) line shows the contribution to the $\delta \mathbf{B}$ energy by the quasiparallel (oblique) modes. (b) The solid black (solid red) line shows the evolution of the electron temperature perpendicular (parallel) to $\langle \mathbf{B} \rangle$. The dashed black (dashed red) line shows the CGL prediction for the perpendicular (parallel) temperature. (c) The black (blue) line shows the energy in the electromagnetic and electrostatic component of δE .

nonthermal electrons, respectively. This is consistent with the fact that before the PEMZ-dominated regime ($t \cdot s \lesssim 2.2$), the three electron populations gain their energy mainly due to AV, as can be seen from the three panels in Figure 6. This means that during this period, energy is gained more efficiently by electron populations with larger average pitch angle. After this, given that the scattering by OQES waves strongly reduces the pitch angle of the nonthermal electrons, their energy gain is no longer related to their $p_{e,\perp}/p_{e,\parallel}$, but to the more efficient acceleration that the PEMZ modes cause on initially more energetic electrons.

5. Comparison with the Compressing Case

In this section we show the effect of driving the $T_{e,\perp} > T_{e,\parallel}$ anisotropy by using compressive instead of shearing simulations. In order to facilitate comparison, the compressing simulations use the same initial conditions as in the shearing case ($f_e \approx 0.53$, $\Theta_e^{\text{init}} = 0.00875$) and are also run until f_e reaches $f_e \approx 2$. In this way, we test whether the transition between the regimes dominated by OQES and PEMZ modes also occur in the compressing runs, and whether this is also accompanied by an increase in the acceleration efficiency. Since in the compressing runs, $\mathbf{v} = -q(y\hat{y} + z\hat{z})/(1 + qt)$, magnetic flux freezing makes the mean magnetic field grow by the same factor as the mean electron density: $(1 + qt)^2$. Thus, in order to make f_e grow from 0.53 to ~ 2 , our compressing simulations run until $tq = 3$. Similarly to our analysis for the shearing simulations, first we describe the interplay between the evolution of the mean magnetic field and the temperature anisotropy. After this, we concentrate on the nonthermal evolution of the electron energy spectrum. We show that although in the compressing case there is significant acceleration driven by the PEMZ modes, this acceleration is less efficient than in the shearing case.

5.1. Anisotropy Regulation in the Compressing Case

Figure 10(a) shows in solid green the growth of the x -component of $\langle \mathbf{B} \rangle$ for simulation C2400 ($\omega_{ce}^{\text{init}}/q = 2400$), which evolves as $|B_x| = |\langle \mathbf{B} \rangle| = B_0(1 + qt)^2$. Because of this

magnetic amplification, initially, $\Theta_{e,\perp}$ and $\Theta_{e,\parallel}$ grow and stay constant, respectively, as seen from the solid black and solid red lines in Figure 10(b). For $t \cdot q \lesssim 1$, $\Theta_{e,\perp}$ and $\Theta_{e,\parallel}$ coincide with the adiabatic CGL evolution shown by the dashed black and dashed red lines, respectively. The departure from the CGL behavior at $t \cdot q \approx 1$ is coincident with the growth and saturation of $\delta \mathbf{B}$, shown by the solid red line in Figure 10(a). This shows that $\Theta_{e,\perp}$ and $\Theta_{e,\parallel}$ are regulated by the pitch-angle scattering provided by temperature-anisotropy-unstable modes, as is the case for the shearing simulations shown in Section 3.

Figures 11(a) and 11(b) show a 2D view of δB_z for the unstable modes in run C2400 at $t \cdot q = 1.5$ (after the saturation of $\delta \mathbf{B}$) and $t \cdot q = 3$, respectively. Although the box initially has a square shape, the effect of compression makes its y -size decrease with time as $1/(1 + qt)$, which explains the progressively more elongated shape of the box shown by the two panels. The dominant modes at $t \cdot q = 1.5$ have wavevectors that are oblique with respect to the direction of the mean magnetic field $\langle \mathbf{B} \rangle$, which is shown by the black arrows. At $t \cdot q = 3$, the waves propagate mainly along $\langle \mathbf{B} \rangle$, which shows that by the end of the simulation, the modes are quasiparallel. The time for the transition between the dominance of oblique to quasiparallel modes can be obtained by calculating the magnetic energy contained in each type of mode. As for the shearing simulations shown in Section 3, we define the modes as oblique (quasiparallel) when the angle between their wavevector \mathbf{k} and $\langle \mathbf{B} \rangle$ is larger (smaller) than 20° . Figure 10(a) shows the magnetic energies in oblique and quasiparallel modes using dashed black and solid black lines, which are denoted by $\langle \delta B_{ob}^2 \rangle$ and $\langle \delta B_{qp}^2 \rangle$, respectively. The oblique modes dominate until $t \cdot s \approx 2$, which corresponds to $f_e \approx 1.6$. After this, the energy in quasiparallel modes dominates the magnetic fluctuations. The existence of these oblique and quasiparallel regimes, and the fact that the transition occurs when $f_e \approx 1.6$, implies that dominance of the different modes is essentially determined by the value of f_e , as was found in the case of the shearing simulations.

Similarly to what occurs in the shearing case, the oblique modes in the compressing runs show significant fluctuations in the electron density n_e . This is shown in Figure 12(a), which

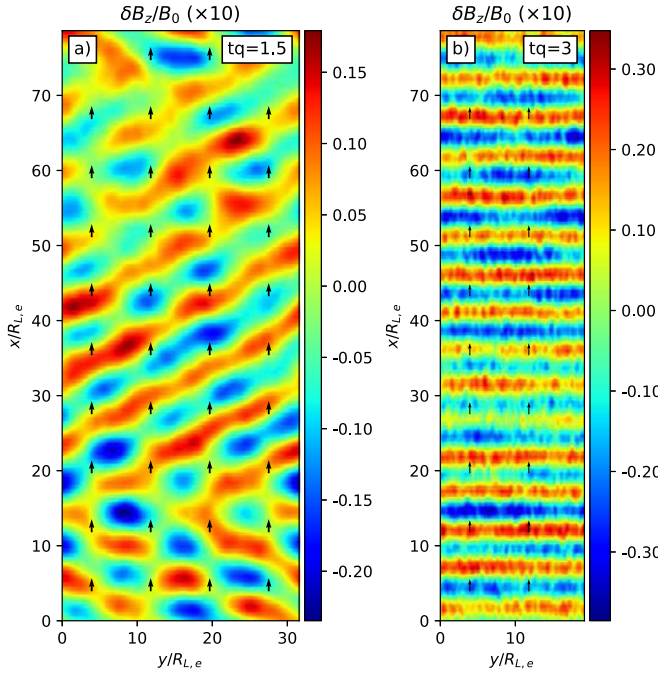


Figure 11. For run C2400 ($\omega_{ce}^{init}/q = 2400$), we show the 2D distribution of δB_z at $t \cdot q = 1.5$ (panel (a)) and $t \cdot q = 3$ (panel (b)), normalized by B_0 . The black arrows show the direction of $\langle \mathbf{B} \rangle$.

shows δn_e at $t \cdot q = 1.5$. The fluctuations in the electron density practically disappear when the quasiparallel modes dominate, as shown by Figure 12(b), which shows δn_e at $t \cdot q = 3$. These different behaviors of δn_e suggest the existence of a significant electrostatic component in the electric field $\delta \mathbf{E}$ when the oblique modes dominate. This is confirmed by Figure 10(c), which shows the energy contained in the electric field fluctuations $\delta \mathbf{E}$ as a function of time, separating it into electrostatic (δE_{es}^2) and electromagnetic (δE_{em}^2) components, which are shown as blue and black lines, respectively. When the oblique modes dominate ($t \cdot q \lesssim 2$), the electric field energy is dominated by δE_{es}^2 ; after this, it gradually becomes dominated by δE_{em}^2 . Figure 10(c) also shows that this transition occurs when the instantaneous $f_e \sim 1.6$ – 1.7 (the instantaneous f_e is shown by the upper horizontal axis), which is fairly similar to the transition seen in the case of shearing simulations at $f_e \sim 1.2$ – 1.5 .

5.2. Electron Acceleration in the Compressing Case

As in the shearing case, PEMZ modes driven by plasma compression also accelerate electrons, although there are some significant differences. Figure 13(a) shows $dn_e/d \ln(\gamma_e - 1)$ for run C2400 at different times $t \cdot q$. We see the rapid growth of a nonthermal tail starting at $t \cdot q \approx 2$. After $t \cdot s \approx 2.5$, this tail can be approximated as a power law of index $\alpha_s \approx 3.7$ with a break at $\gamma_e - 1 \sim 1$, where the spectrum becomes significantly steeper. The fact that most of the nonthermal behavior starts when the PEMZ modes become dominant ($t \cdot q \sim 2$) suggests that as in the shearing case, the nonthermal acceleration is mainly driven by the PEMZ modes.

One significant difference between the shearing and compressing case is that the latter gives rise to a softer nonthermal component in the final electron energy spectrum than the former (a power law of index $\alpha_s \approx 3.7$ instead of $\alpha_s \approx 2.9$). This difference is not surprising given that the

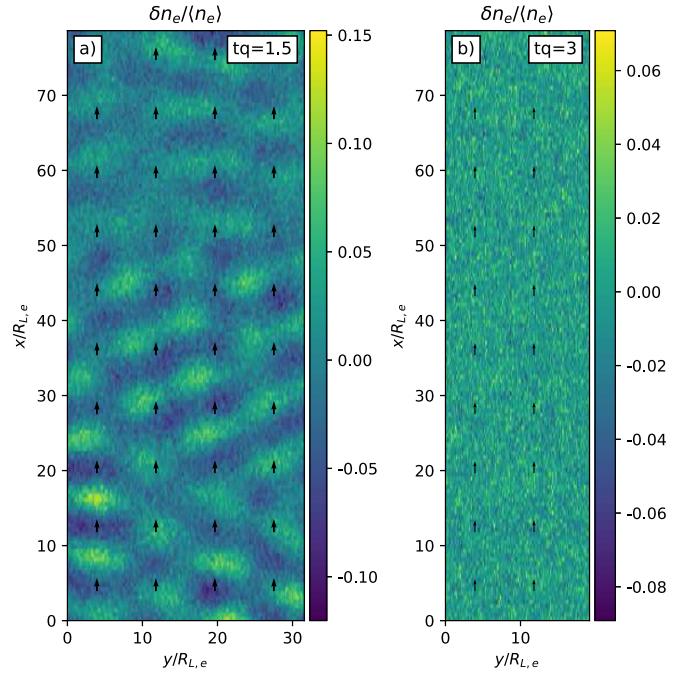


Figure 12. Same as Figure 11, but for the electron density fluctuations δn_e , normalized by the average density $\langle n_e \rangle$.

overall electron energy gain when f_e evolves from $f_e = 0.53$ and $f_e \approx 2$ is significantly higher for the compressing runs. While in the shearing case, the final value of $\Theta_{e,\perp}$ is about 3 times higher than its initial value (see the solid black line in Figure 1(b)), in the compressing case, the final $\Theta_{e,\perp}$ is about 10 times higher than the initial $\Theta_{e,\perp}$ (see the solid black line in Figure 10(b)). Because at the end of both types of simulations $\Theta_{e,\perp} \gg \Theta_{e,\parallel}$, this difference implies that by the end of the compressing runs, the electrons are significantly hotter than in the shearing runs. The different electron internal energies may affect the efficiency with which electrons gain energy from their interaction with the PEMZ modes, as has been shown by previous quasilinear theory studies of the stochastic acceleration of electrons by whistler/z modes (Summers et al. 1998). This implies that shearing and compressing runs that start with the same electron parameters should not necessarily produce equally hard nonthermal component in the electron spectrum after f_e has increased from 0.53 to ~ 2 .

Figure 13(b) shows a numerical convergence test of the final spectrum at $t \cdot q = 3$. It compares run C2400 ($d_e^{init}/\Delta x = 50$, $N_{epc} = 200$, and $L/R_{Le}^{init} = 78$) with a run with $d_e^{init}/\Delta x = 40$ (run C2400a, dotted blue line), a run with $N_{epc} = 100$ (run C2400b, dotted red line), and a run with $L/R_{Le}^{init} = 39$ (run C2400c, dotted green line). No significant difference can be seen between the different spectra, with only a slight hardening for the highest-resolution run C2400, which implies that our results are reasonably well converged numerically.

The effect of varying ω_{ce}^{init}/q is investigated in Figure 13(c), where the final spectra ($t \cdot q = 3$) are shown for runs with $\omega_{ce}^{init}/q = 300, 600, 1200,$ and 2400 (runs C300, C600, C1200, and C2400, respectively). As ω_{ce}^{init}/q increases, there is a hardening of the low-energy part of the nonthermal tail ($0.3 \lesssim \gamma_e - 1 \lesssim 0.8$), which converges toward a power-law tail of index $\alpha_s \approx 3.7$ with little difference between the cases with $\omega_{ce}^{init}/q = 1200$ and 2400 . Additionally, as ω_{ce}^{init}/q increases, there is a decrease in the prominence of a high-energy bump at

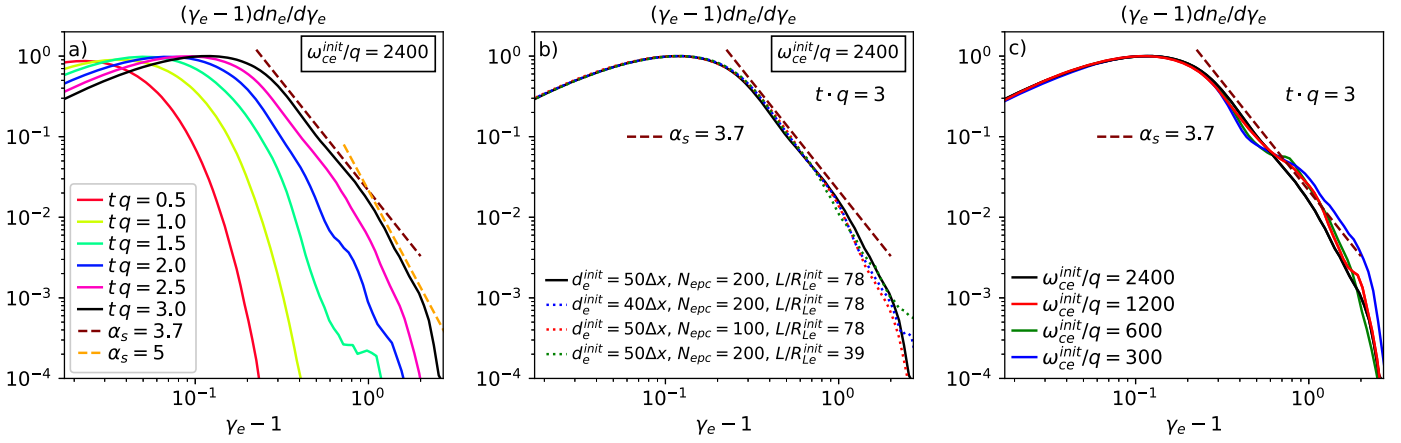


Figure 13. (a) The electron energy spectrum for run S1200 for different values of $t \cdot q$, where γ_e is the electron Lorentz factor. The dashed brown line shows a power law of index $\alpha_s \approx 3.7$, which at $t \cdot q \approx 2.5$ – 3 resembles the nonthermal tail up to a break at $\gamma_e \sim 1$. (b) Test of numerical convergence of the final spectrum ($t \cdot q = 3$). We compare run C2400 (solid black; $d_e^{\text{init}}/\Delta x = 50$, $N_{\text{epc}} = 200$, $L/R_{Le}^{\text{init}} = 78$) with runs using (i) a lower time and space resolution $d_e^{\text{init}}/\Delta x = 40$ (run C2400a, dotted blue line), (ii) a smaller $N_{\text{epc}} = 100$ (run C2400b, dotted red line), and (iii) a smaller box size $L/R_{Le}^{\text{init}} = 39$ (run C2400c, dotted green line). No significant difference can be seen between the different spectra, except for the highest-resolution run C2400 having a slightly harder spectrum. (c) The final electron spectra for runs C2400 (black), C1200 (red), C600 (green), and C300 (blue).

$\gamma_e - 1 \sim 1$, which essentially disappears for $\omega_{ce}^{\text{init}}/q = 2400$. This suggests that the magnetizations $\omega_{ce}^{\text{init}}/q$ used in our compressing runs provide a reasonable approximation to the expected spectral behavior in realistic flare environments.

6. Possible Role of Collisions

In this work, we have assumed a negligible role of Coulomb collisions between electrons. We validate this assumption by calculating the Coulomb collision rate ν_{ee} for electrons with temperature T_e and density n_e (Spitzer 1962),

$$\nu_{ee} \approx 0.2 \text{ s}^{-1} \left(\frac{n_e}{10^9 \text{ cm}^{-3}} \right) \left(\frac{T_e}{50 \text{ MK}} \right)^{-3/2}, \quad (5)$$

where we have assumed a Coulomb logarithm of 20 (appropriate for $n_e \approx 10^9 \text{ cm}^{-3}$ and $T_e \approx 50 \text{ MK}$). Because for our fiducial parameters $n_e \approx 10^9 \text{ cm}^{-3}$ and $T_e \approx 50 \text{ MK}$, ν_{ee} is significantly smaller than the rate at which temperature anisotropy growth would be driven in contracting loop tops ($s \sim 1 \text{ s}^{-1}$ for $B \sim 100 \text{ G}$, as we estimated in Section 4.2), our collisionless approach is valid in the low-density cases ($n_e \sim 10^8$ – 10^9 cm^{-3}). However, Equation (5) shows that for $n_e \gtrsim 10^{10} \text{ cm}^{-3}$, collisions could become dominant, probably reducing the efficiency of the electron acceleration.

7. Summary and Conclusions

Using 2D particle-in-cell plasma simulations, we study the effect of temperature anisotropy instabilities on electron acceleration under conditions suitable for ALT regions in solar flares. In our simulations, we drove the growth of a $T_{e,\perp} > T_{e,\parallel}$ anisotropy using the adiabatic invariance of the electron magnetic moment μ_e in a growing magnetic field B , which is achieved by imposing either a shearing or a compressing plasma motion. In both cases, when the difference between $T_{e,\perp}$ and $T_{e,\parallel}$ is large enough, different plasma modes become unstable, and through pitch-angle scattering, limit the anisotropy growth. Because B grows continuously in our simulations, our setup drives the instabilities into their nonlinear, saturated regime, allowing the $T_{e,\perp}$ and $T_{e,\parallel}$ anisotropy to

self-regulate and capturing the long-term effect of the instabilities on the electron spectra.

Our study considers an initial electron temperature $T_e \approx 52 \text{ MK}$ and an electron density and magnetic field B such that f_e evolves from $f_e \approx 0.53$ to ≈ 2 . Our results are summarized as follows:

1. Both in the shearing and compressing runs, electrons are efficiently accelerated mainly by the inelastic scattering provided by unstable PEMZ modes, which dominate for $f_e \gtrsim 1.2$ – 1.7 . This acceleration corresponds to a transfer of energy from the electrons in the thermal part of the spectrum to the electrons in the nonthermal tail, with the PEMZ modes playing the role of carriers of that energy. When $f_e \lesssim 1.2$ – 1.7 , pitch-angle scattering is mainly provided by OQES modes and the nonthermal acceleration is rather inefficient.
2. By the end of the shearing runs, the spectrum contains a nonthermal tail that can be approximated as a power law of index $\alpha_s \approx 2.9$, in addition to a high-energy bump that reaches energies of $\sim 300 \text{ keV}$. By the end of the compressing runs, the spectrum has an approximate power-law tail of index $\alpha_s \approx 3.7$, with a break at $\sim 500 \text{ keV}$; at higher energies, $\alpha_s \sim 5$ (as shown by the dashed orange line in Figure 13(a)). This difference between the shearing and compressing runs is as expected given the different evolution of electron temperatures in these two types of runs.
3. Our results are largely independent of the ratios ω_{ce}/s or ω_{ce}/q when these ratios are sufficiently high. This implies that our study can be extrapolated to realistic solar flare conditions, where ω_{ce}/s or ω_{ce}/q should be several orders of magnitude larger than in our simulations.




In conclusion, our simulations show that under conditions expected in ALT sources, electron temperature anisotropy instabilities have the potential of contributing to the acceleration of electrons, probably as a complement to the acceleration processes expected in reconnection current sheets in solar flares. Interestingly, the spectral index observed from our shearing runs ($\alpha_s \approx 2.9$) is within the range of inferred indices in some ALT sources (e.g., Alexander & Metcalf 1997). Also,

the spectral index obtained from our compressing runs ($\alpha_s \approx 3.7$) agrees reasonably well with the spectral index $\alpha_s \approx 3.6$ inferred from multiwavelength observations of the ALT source in the X8.2-class solar flare of 2017 September 10 (Chen et al. 2021). In this flare, the power-law tail shows a break at ~ 160 keV, and at higher energies, $\alpha_s \sim 6$. This feature is qualitatively similar to the spectral breakdown observed in our compressing runs, although in our simulations, the break occurs at ~ 500 keV, with $\alpha_s \sim 5$ at higher energies.

We point out, however, that the present study is not intended to make precise predictions regarding observationally inferred nonthermal electron tails in ALT sources. Indeed, the anisotropy driving implemented in this work constitutes a simplified local model for the way the electron velocity distribution may evolve in ALT sources. A global description should consider the electron ability to escape the loop-top region (which may give rise to a loss-cone velocity distribution with $T_{e,\perp} > T_{e,\parallel}$; (e.g., Fleishman & Melnikov 1998), as well as a more realistic prescription for the magnetic field evolution. Also, the initial values of f_e and T_e chosen in this work, although appropriate for ALT sources, do not represent the whole range of possible conditions in these environments. For these reasons, we consider this study a first step in assessing the possible role of electron temperature anisotropy instabilities in accelerating electrons in solar flares, under specific initial conditions and assuming that this anisotropy is driven by either shearing or compressing plasma motions. We defer the study of the effect of a wider range of initial plasma conditions as well as of the global loop dynamics to future works.

M.R. thanks for support from Fondecyt Regular grant No. 1191673. A.O. acknowledges support from Beca EPEC-FCFM. D.V. is supported by the STFC Ernest Rutherford Fellowship ST/P003826/1 and STFC Consolidated Grant ST/S000240/1. This research was supported in part by the National Science Foundation under grant No. NSF PHY-1748958. Most of the numerical simulations included in this work were performed at the National Laboratory for High Performance Computing (NLHPC) of the Center for Mathematical Modeling of University of Chile (ECM-02).

ORCID iDs

Mario Riquelme  <https://orcid.org/0000-0003-2928-6412>
 Daniel Verscharen  <https://orcid.org/0000-0002-0497-1096>
 Lorenzo Sironi  <https://orcid.org/0000-0002-1227-2754>

References

- Abdul, R. F., Matthews, A. P., & Mace, R. L. 2021, *PhPI*, **28**, 062104
 Alexander, D., & Metcalf, T. 1997, *ApJ*, **489**, 442
 An, X., Yue, C., Bortnik, J., et al. 2017, *JGRA*, **122**, 2001
 Arnold, H., Drake, J. F., Swisdak, M., et al. 2021, *PhRvL*, **126**, 135101
 Benz, A. O. 2017, *LRSP*, **14**, 2
 Benz, A. O., & Gudel, M. 2010, *ARA&A*, **48**, 241
 Buneman, O. 1993, *Computer Space Plasma Physics*, 67 (Tokyo: Terra Scientific), 67
 Cai, Q., Shen, C., Raymond, J. C., et al. 2019, *MNRAS*, **489**, 3183
 Cairns, I. H., Lobzin, V. V., Donea, A., et al. 2018, *NatSR*, **8**, 1676
 Chang, O., Gary, S. P., & Wang, J. 2013, *JGRA*, **118**, 2824
 Che, H., & Zank, G. P. 2020, *ApJ*, **889**, 11
 Che, H., Zank, G. P., Benz, A. O., Tang, B., & Crawford, C. 2021, *ApJ*, **908**, 72
 Chen, B., Bastian, T. S., Shen, C., et al. 2015, *Sci*, **350**, 1238
 Chen, B., Battaglia, M., Krucker, S., Reeves, K., & Glesener, L. 2021, *ApJ*, **908**, L55
 Chen, B., Shen, C., Gary, D. E., et al. 2020, *NatAs*, **4**, 1140
 Chen, B., Shen, C., Reeves, K., Guo, F., & Yu, S. 2019, *ApJ*, **884**, 63
 Chew, G. F., Goldberger, M. L., & Low, F. E. 1956, *RSPSA*, **236**, 112
 Dahlin, J. T. 2020, *PhPI*, **27**, 100601
 Drake, J. F., Shay, M. A., Thongthai, W., & Swisdak, M. 2005, *PRL*, **94**, 095001
 Drake, J. F., Swisdak, M., Che, H., & Shay, M. A. 2006, *Natur*, **443**, 553
 Drake, J. F., Swisdak, M., & Fermo, R. 2013, *ApJL*, **763**, L5
 Du, S., Guo, F., Zank, G. P., Li, X., & Stanier, A. 2018, *ApJ*, **867**, 16
 Egedal, J., Daughton, W., & Le, A. 2012, *NatPh*, **8**, 321
 Feldman, U., Hiei, E., Phillips, K. J. H., Brown, C. M., & Lang, J. 1994, *ApJ*, **421**, 843
 Fleishman, G. D., & Melnikov, V. F. 1998, *PhyU*, **41**, 1157
 Fletcher, L., Dennis, B. R., Hudson, H. S., et al. 2011, *SSRv*, **159**, 19
 Forbes, T. G. 2013, *NatPh*, **9**, 456
 Gary, S. P., & Cairns, I. H. 1999, *JGR*, **104**, 19835
 Gary, S. P., Liu, K., & Winske, D. 2011, *PhPI*, **18**, 082902
 Gou, T., Veronig, A. M., Dickson, E. C., Hernandez-Perez, A., & Liu, R. 2017, *ApJ*, **845**, L1
 Hamilton, R. J., & Petrosian, V. 1992, *ApJ*, **398**, 350
 Karlicky, M., & Kosugi, T. 2004, *A&A*, **419**, 1159
 Klein, K., & Dalla, S. 2017, *SSRv*, **212**, 1107
 Kliem, B. 1994, *ApJS*, **90**, 719
 Kong, X., Guo, F., Shen, C., et al. 2020, *ApJ*, **905**, L16
 Kulsrud, R. M. 1983, in *Handbook of Plasma Physics*, ed. M. N. Rosenbluth & R. Z. Sagdeev (Amsterdam: North-Holland), 115
 Kuridze, D., Mathioudakis, M., Morgan, H., et al. 2019, *ApJ*, **874**, 126
 Le Roux, J. A., Zank, G. P., Webb, G. M., & Khabarova, O. 2015, *ApJ*, **801**, 112
 Lee, S., Lee, E., Seough, J., et al. 2018, *JGRA*, **123**, 3277
 Ley, F., Riquelme, M., Sironi, L., Verscharen, D., & Sandoval, A. 2019, *ApJ*, **880**, 100
 Li, X., Guo, F., Li, H., & Li, G. 2017, *ApJ*, **843**, 21
 Li, X., Guo, F., Li, H., Stanier, A., & Kilian, P. 2019, *ApJ*, **884**, 118
 Li, X., Guo, F., & Liu, Y. 2021, *PhPI*, **27**, 052905
 Liu, W., Petrosian, V., Dennis, B. R., & Jiang, Y. W. 2008, *ApJ*, **676**, 704
 Luo, Y., Chen, B., Yu, S., Bastian, T., & Krucker, S. 2021, *ApJ*, **911**, 4
 Masuda, S., Kosugi, T., Hara, H., et al. 1995, *PASJ*, **47**, 677
 Masuda, S., Kosugi, T., Hara, H., Tsuneta, S., & Ogawara, Y. 1994, *Natur*, **371**, 495
 Melrose, D. B. 1974, *SoPh*, **37**, 353
 Miller, J., Cargill, P., Emslie, A., et al. 1997, *JGR*, **102**, 14631
 Miller, J. A. 1997, *ApJ*, **491**, 939
 Miller, J. A., Larosa, T. N., & Moore, R. L. 1996, *ApJ*, **461**, 445
 Miller, J. L. 2013, *PhT*, **66**, 12
 Minoshima, T., Masuda, S., & Miyoshi, Y. 2010, *ApJ*, **714**, 332
 Minoshima, T., Masuda, S., Miyoshi, Y., & Kusano, K. 2011, *ApJ*, **732**, 111
 Oka, M., Birn, J., Battaglia, M., et al. 2018, *SSRv*, **214**, 82
 Petrosian, V. 2012, *SSRv*, **173**, 535
 Petrosian, V., & Liu, S. 2004, *ApJ*, **610**, 550
 Pongkitiwanchakul, P., & Chandran, B. D. G. 2014, *ApJ*, **796**, 45
 Riquelme, M. A., Osorio, A., & Quataert, E. 2017, *ApJ*, **850**, 113
 Riquelme, M. A., Quataert, E., Sharma, P., & Spitkovsky, A. 2012, *ApJ*, **755**, 50
 Riquelme, M. A., Quataert, E., & Verscharen, D. 2015, *ApJ*, **800**, 27
 Riquelme, M. A., Quataert, E., & Verscharen, D. 2016, *ApJ*, **824**, 123
 Riquelme, M. A., Quataert, E., & Verscharen, D. 2018, *ApJ*, **854**, 132
 Sharma, P., Quataert, E., Hammett, G., & Stone, L. 2007, *ApJ*, **667**, 714
 Shen, C., Kong, X., Guo, F., Raymond, J. C., & Chen, B. 2018, *ApJ*, **869**, 116
 Sironi, L. 2015, *ApJ*, **800**, 89
 Sironi, L., & Narayan, R. 2015, *ApJ*, **800**, 88
 Snyder, P. B., Hammett, G. W., & Dorland, W. 1997, *PhPI*, **4**, 3974
 Spitkovsky, A. 2005, in *AIP Conf. Proc. 801, Astrophysical Sources of High Energy Particles and Radiation* (Melville, NY: AIP), 345
 Spitzer, L., Jr. 1962, *Physics of Fully Ionized Gases* (2nd ed; New York: Interscience)
 Stverak, S., Travnicek, P., Maksimovic, M., et al. 2008, *JGRA*, **113**, A03103
 Su, Y., Veronig, A. M., Holman, G. D., et al. 2013, *NatPh*, **9**, 489
 Summers, D., Thorne, R. M., & Xiao, F. 1998, *JGR*, **103**, 20487
 Takasao, S., Matsumoto, T., Nakamura, N., & Shibata, K. 2015, *ApJ*, **805**, 135
 Tao, X., & Lu, Q. 2014, *PhPI*, **21**, 022901
 Tsuneta, S., Masuda, S., Kosugi, T., & Sato, J. 1997, *ApJ*, **478**, 787
 Verscharen, D., & Chandran, B. 2018, *RNAAS*, **2**, 13
 Wang, H., Lu, Q., Huang, C., & Wang, S. 2016, *ApJ*, **821**, 84
 Wang, J., Simões, P. J. A., Jeffrey, N. L. S., et al. 2017, *ApJ*, **847**, L1
 Xia, Q., Dahlin, J., Zharkova, V., & Antiochos, S. 2020, *ApJ*, **894**, 89
 Zhang, Q., Guo, F., Daughton, W., Li, X., & Li, H. 2021, *PhRvL*, **127**, 185101
 Zhu, C., Liu, R., Alexander, D., & McAteer, R. T. J. 2016, *ApJ*, **821**, L29